48th AIAA Aerospace Sciences Meeting Including the New Horizons Forum and Aerospace Exposition
4 - 7 January 2010, Orlando, Florida

AIAA 2010-1053

Design and Performance of Circulation Control Flap Systems

Rory M. Golden* and David D. Marshall†
California Polytechnic State University, San Luis Obispo, CA, 93407-0352

The design of circulation control (CC) dual radius flap systems were investigated to characterize the parameters that make up the flap surface to offer further knowledge into the CC field of study. Multiple dual radius flap geometries, along with variants, were developed by varying specific flap parameters from a baseline configuration that had previously developed. The aerodynamics of the different flap geometries were analyzed using two-dimensional CFD. This research will explore the design of CC pneumatic flap systems to improve the performance of existing CC flap configurations, and provide insight into the characteristics of the CC flap geometry.

Nomenclature

α	=	angle of attack (°)	$\dot{m}_{slot}$	=	2-D mass flow rate (kg/(m*s))
A	=	area of slot exit (m^2)	M	=	slot Mach
A*	=	critical area of slot exit (m^2)	M_∞	=	freestream Mach
c	=	chord length (m)	μ_∞	=	freestream dynamic viscosity (kg/(m*s))
c'	=	flap modified chord length (m)	P_∞	=	freestream pressure (Pa)
c_f	=	flap chord length (m)	P_{slot}	=	slot local static pressure (Pa)
C_d	=	drag coefficient	P_{stag}	=	slot stagnation pressure (Pa)
C_f	=	skin friction coefficient	ρ_∞	=	freestream density (kg/m^3)
C_l	=	2-D lift coefficient	q_∞	=	freestream dynamic pressure ($kg/(m*s^2)$)
$C_{m,\,(c/4)}$	=	quarter-chord moment coefficient	r_1	=	first radial arc of CC flap (m)
C_μ	=	momentum coefficient	r_2	=	second radial arc of CC flap (m)
C_p	=	pressure coefficient	$r_{2\ avg}$	=	average second radius of CC flap (m)
γ	=	ratio of specific heats	R_∞	=	freestream gas constant(J/(kg*K))
δ_f	=	flap deflection (°)	T_∞	=	freestream temperature (K)
ε	=	turbulence dissipation rate	T_{slot}	=	slot local static temperature (K)
f	=	elliptic relaxation factor	T_{stag}	=	slot stagnation temperature (K)
h_{slot}	=	trailing edge slot height (m)	v^2	=	velocity scale
θ	=	departure angle from upper surface (°)	V_{slot}	=	slot velocity (m/s)
k	=	turbulence kinetic energy	x	=	chord-wise direction (m)
κ	=	curvature	y+	=	dimensionless wall distance
L/D	=	lift-to-drag ratio	ω	=	specific dissipation

I. Introduction

Development of circulation control (CC) flap systems has long been part of a vision for next-generation subsonic transport aircraft, offering significant payoffs in both performance and in system complexity[1]. CC flap systems augment aerodynamic forces by entraining and deflecting the airfoil flow field pneumatically, rather than solely by deflecting a mechanical surface[2]. The use of pneumatic devices in the form of blown jet airfoils in aerodynamics have been under investigation as far back as the 1930's, and possibly earlier[2]. A Romanian inventor, by the name of Henri Coanda, discovered the phenomena of CC (claimed to be in 1910) in a near-fatal plane crash where the exhaust deflection plates he developed entrained the hot flow and directed onto the aircraft, causing it to ignite[3]. The concept of CC entails ejecting high momentum, jet flow out of a slot located near the trailing edge of an airfoil, shown in Figure 1[4]. The slot emits this air over a curved or radial surface. The high momentum flow follows the

* Graduate Student, Department of Aerospace Engineering, Student Member AIAA.
† Associate Professor, Department of Aerospace Engineering, Senior Member AIAA.

curved surface due to both the sub-ambient pressure of the jet flow and the centrifugal force created by the curved surface, a phenomena which is known as the Coanda effect. The airflow over the wing is then entrained over the curved surface by the pressure gradient caused by the high momentum air. This lowers both, leading and trailing edge, stagnation points to the bottom surface of the wing, increasing effective camber which increases circulation. Figure 2[5] presents the streamlines encountered during the operation of a CC flap. The increased circulation has been seen to produce two-dimensional lift coefficients (C_l) upwards of 7 and 10[6]. It has been demonstrated that CC flap systems can produce substantial lift gains over the conventional flapped airfoil[7,8]. The CC flaps can also be coupled with over-the-wing engine configurations to provide even greater lifting capability, turning engine thrust well past 90° from the horizontal[2].

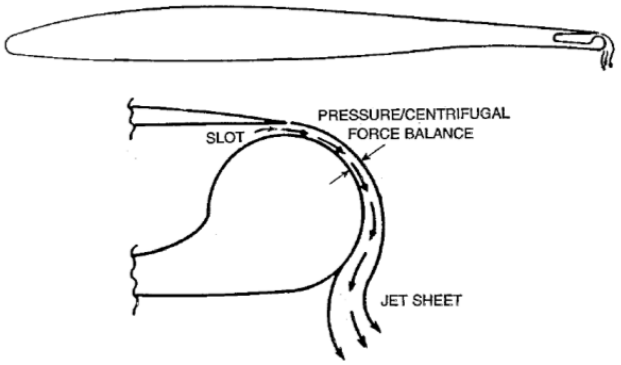

Figure 1. CC with Coanda effect over trailing edge[4].

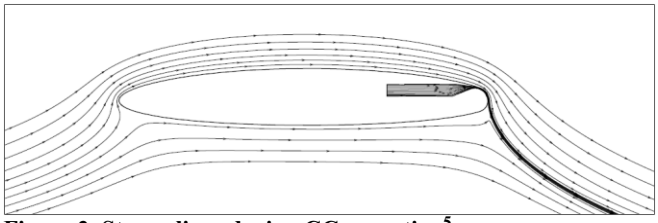

Figure 2. Streamlines during CC operation[5].

The area of application of the CC flaps will be on an N+2 (expected 2018-2022) cruise efficient short takeoff and land (CESTOL) 100 passenger airliner developed for a NASA research grant[9], advanced model for extreme lift and improved aero-acoustics (AMELIA), to validate CFD's predictive capability with a large-scale wind tunnel test, which is displayed in Figure 3. Table 1 presents the desired goals set forth by NASA[10] for an N+2 design, like AMELIA.

Figure 3. N+2 CESTOL design for AMELIA.

Table 1. NASA N+2 goals[10].

NASA Goals for N+2 100 Passenger Airliner	
→	Balanced field length of 2,000 feet
→	Efficient cruise at Mach 0.8
→	Takeoff and land speeds less than 50 knots
→	Turn radius in terminal area less than 0.25 nm
→	1400 - 2000 mile range
→	Noise footprint within the airport boundary

A three view of the AMELIA design is displayed in Figure 4 below. The decision for CC flaps on the aircraft was chosen due to the efficiency of the CC flaps when compared to other blown high lift systems in the $\Delta C_l/\Delta C_\mu$ values, which are presented in Figure 5[11] below. AMELIA will incorporate leading edge blowing as well to prevent upper surface separation of the airfoil, which has been experienced in flight tests of a CC flap system[12]. The leading edge slot has been proven experimentally[13] and has shown greater performance in increasing stall α over more complex mechanical leading edge devices[1]. The CC slot air for this configuration will be provided by an auxiliary power unit (APU), which will not require engine bleed to feed the slots which result thrust losses during flap

operation and oversize the engines. This APU could also be used for heating/air conditioning or pressurization when it isn't needed to power the flap system[14]. The CC flap system employed on the AMELIA design will incorporate slots that will retract when the system is not in operation, to provide decreased cruise drag which is important for optimizing fuel burn[15]. The CC flaps provide many benefits to the AMELIA design; a less complex flap system, increased lift from over-the-wing engine exhaust entrainment, and a better performing flap that will result in shorter takeoff and landing distances, steeper climb-out and approach angles that reduce community noise, and decreased cruise drag. The use of CC flaps have also shown to be more acoustically acceptable than conventional mechanical flaps[16], by eliminating the vortex shedding in the trailing edge region of the airfoil.

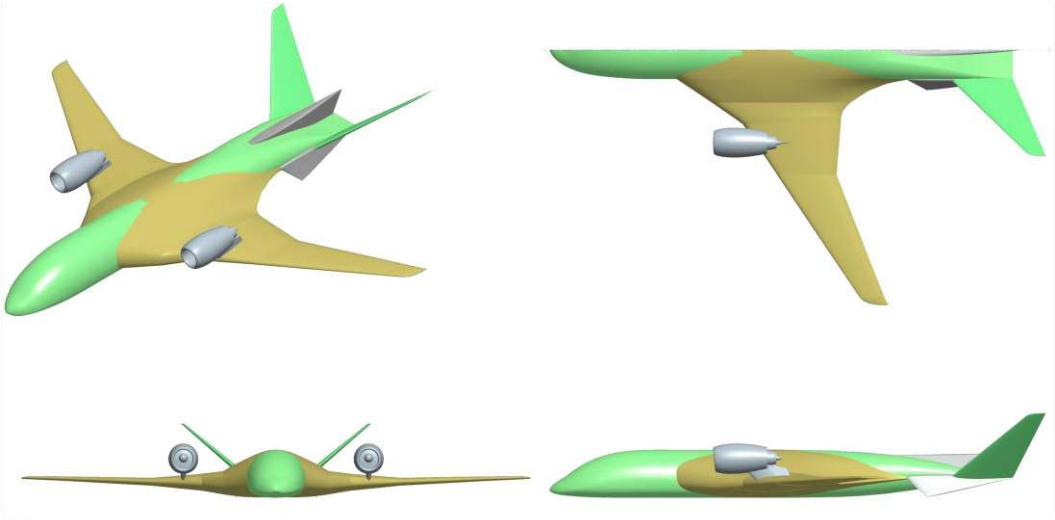

Figure 4. Three-view of AMELIA model.

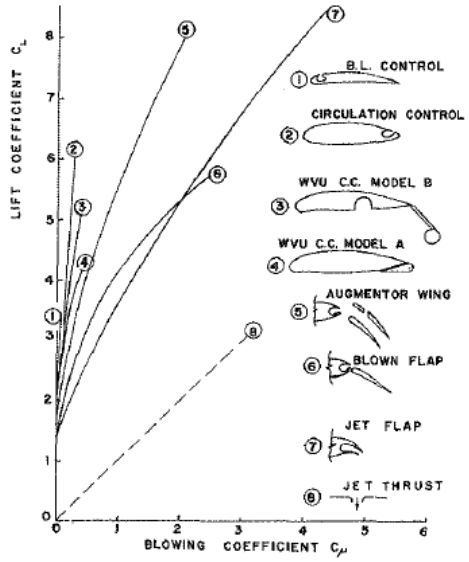

Figure 5. Flap efficiency for various blown high-lift systems[11].

Supercritical airfoils have been the most successful in the integration of the CC dual radius flaps. The large leading edge radius helps in keeping flow attached during CC operation, and provides sufficient space for any leading edge devices. The trailing edge thickness of the supercritical geometry accommodates both the trailing edge slot plenum along with the radial surfaces of the flap[17]. The transonic cruise performance of the supercritical airfoil is also desirable, delaying shock-induced drag. The NASA SC(2)-0414 (Figure 6) was the airfoil chosen for the analysis, being the most similar to AMELIA's airfoil.

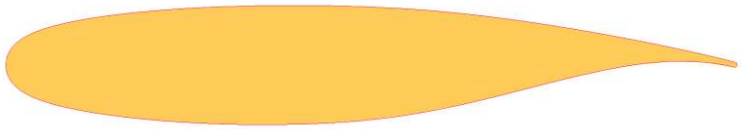

Figure 6. NASA SC(2) - 0414 airfoil.

Of the exiting CC flap configurations that have been developed (displayed in Figure 7[12]), the dual radius will be the configuration further investigated. The dual radius flap first acquires the benefit of the smaller radius by turning the slot flow over a larger angle in a smaller chord-wise distance, which occurs because of the high momentum the flow still carries from being ejected from the slot. It then takes advantage of the larger radius to keep the flow attached as it travels along the flap and its high momentum energy is reduced[17]. The dual radius also employs a sharp trailing edge which increases the jet thrust recovery during deployment and operation and greatly reduces the pressure drag in cruise configuration[17]. These contributions render the dual radius the best performing CC flap configuration of the existing designs, thus making it the baseline flap to be developed in the forthcoming analysis.

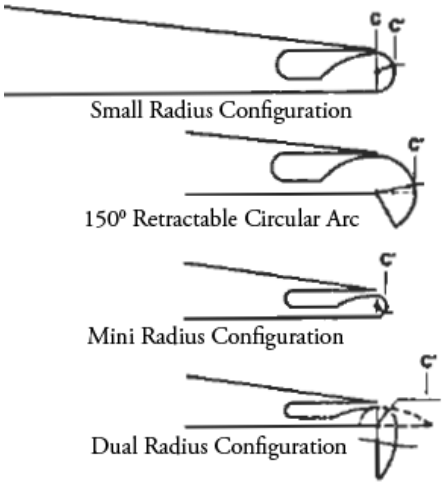

Figure 7. CC flap configurations[12].

II. CC Flap Geometry and Design

Figure 8 below describes the defining geometry of the CC flap to be investigated.

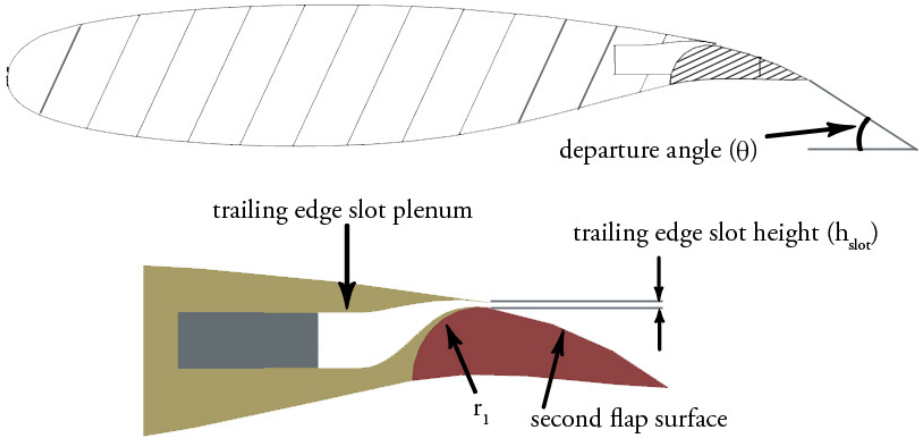

Figure 8. CC flap geometry.

Due to the importance of entraining the flow over the top of the wing using the high momentum air on the Coanda/flap surface, this design study explores the impact of the geometry of the flap on the aerodynamic performance of the CC flap system. In doing so, the leading edge slot will not be incorporated into this analysis, isolating the performance characteristics to be solely effected by the changes in the aft flap geometry. The baseline CC dual radius flap configuration was designed to specifications developed by previous research[18]. To create an effective dual radius flap, Figure 9[18] was followed in defining the trailing edge slot height (h_{slot}) and radius of the first radius (r_1) of the dual radius flap. The design point was chosen to aid in the manufacturing of the wind tunnel model's slots, along with keeping the flap within the region of most effective Coanda operation. The flap was designed to r_1 because it is the first radius that the slot flow will encounter when the flap is deflected. The chord was chosen to be the mean aerodynamic chord of the design. The baseline flap parameters are presented in Table 2. Due to the importance of capturing the correct flow in the region of the flap, the plenum was also incorporated into the model. This allowed for proper flow characteristics of the slot flow, allowing the boundary layer to grow from the plenum inlet, throughout the slot, and onto the flap surface.

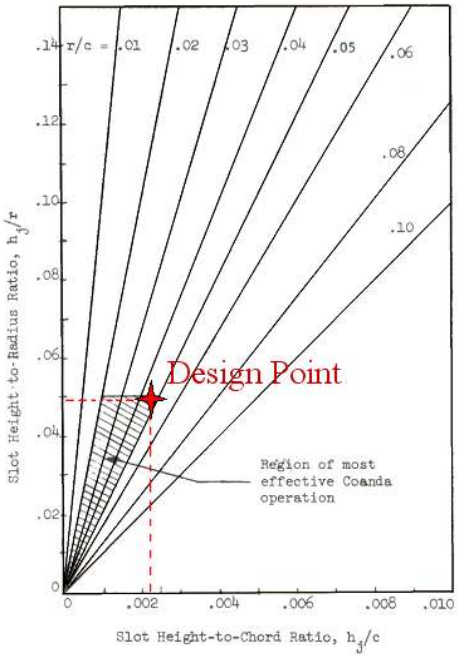

Figure 9. CC Coanda performance[18].

Table 2. Baseline CC flap design parameters.

c (m)	0.47370
h_{slot}/c	0.00238
r_1/c	.04857
h_{slot}/r_1	.04900

To place the flap on the airfoil (Figure 10a.), several constraints were enforced. The first, having a circular arc of radius r_1 intersect the upper and lower surface of the aft part of the airfoil (Figure 10b.). The upper intersection was then constrained to have the circular arc become tangent with the upper surface of the airfoil (Figure 10c.). The circular arc of r_1 is then constrained to be perpendicular to the horizontal at the lower intersection of the airfoil (Figure 10d.), which finalizes the flap's chord-wise placement. The second flap surface is then extended from the top end point of the first r_1 arc, being tangentially constrained to it (Figure 10e.). The second flap surface is then extended to the specified length, and ending on the airfoil's chord line (Figure 10f.). A spline is then added between the end of the second flap surface and the start point of the r_1 arc on the bottom of the airfoil and constrained to be tangent to the existing airfoil at that location (Figure 10g.). Figure 10h. shows the completed flap integration for one of the analyzed flap configurations.

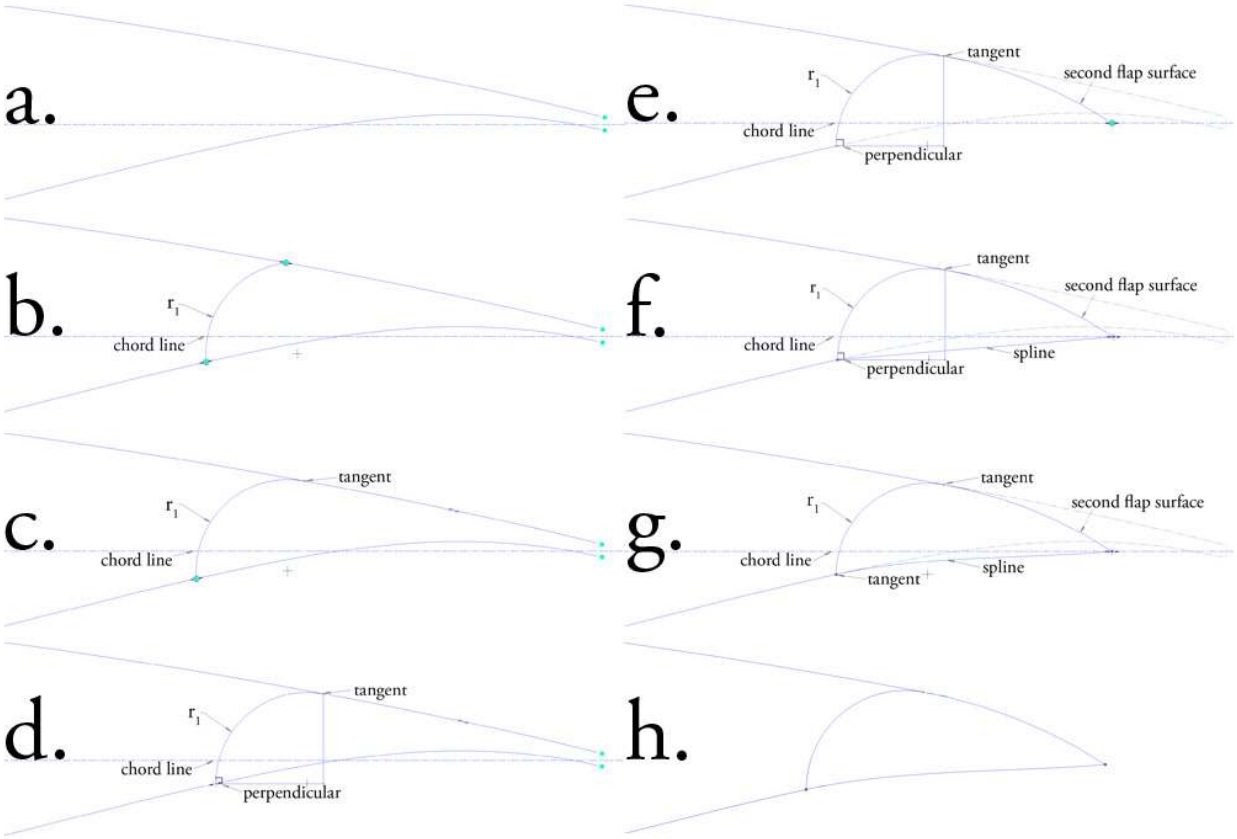

Figure 10. Flap placement.

To create the trailing edge slot on the airfoil, a vertical element was added at the location of the flap's intersection of the upper surface. The element has a height of h_{slot} plus an additional 0.254 mm, to account for the upper surface material that will be encountered. To keep the continuity of the upper airfoil surface with the slot and to ensure mechanical feasibility, a spline was added from 55% chord of the airfoil to the slot location. This spline was constrained to be tangent to the airfoil surface at 55% chord and to be parallel to the tangent of the airfoil surface below the slot. Figure 11 depicts the modification of the airfoil to accommodate the trailing edge slot. Once this process of modifying the airfoil takes place, the CC dual radius flap system will be placed and incorporated onto the airfoil of interest.

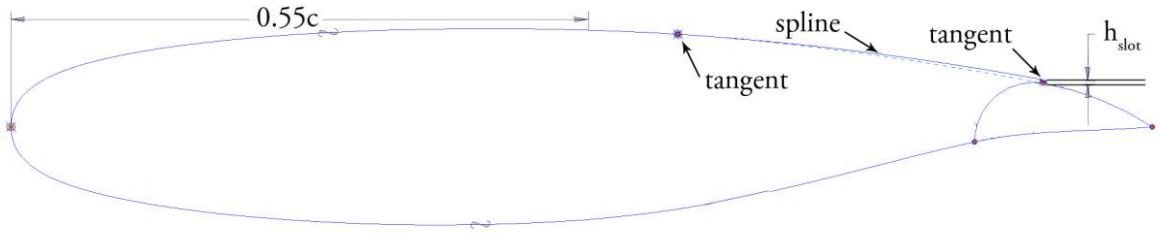

Figure 11. Trailing edge slot modification.

III. Parameter Studies

Due to the emphasis on the geometrical design of the CC dual radius flap system, some of the parameters of the flap were held constant throughout the analysis. The first of which was the two-dimension slot jet momentum coefficient ($C\mu$), which is the driving parameter in the lift augmentation ($\Delta C_l/C_\mu$) of the CC operation. The other parameters that were held constant were the flap location (chord wise-direction), slot location, slot height, the plenum shape, and the first radial surface of the flap, r_1. This left the flap surface aft of the r_1 arc to be further investigated, detailed in Figure 12.

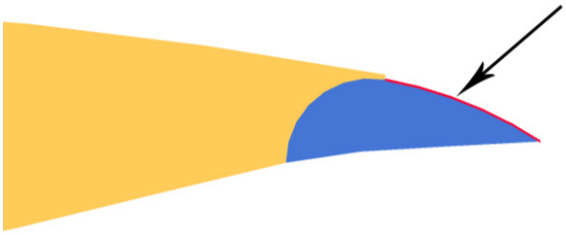

Figure 12. Aft segment of flap surface.

A. Preliminary Dual Radius Study

The parameters of interest in this research were initially the second radius (r_2) and the length of strictly the dual radius flap configurations. The first of the parameters that was studied was length of the dual radius flap which had a direct influence on the departure angle (θ) due to the previous constraints that placed the flap. By changing the length of the flap or θ, it influenced the turning angle of the flow. By having a shorter flap with a greater θ, it was predicted that the flow would be influenced to more turning by the decreased radius of the curved surface, but also have more difficulty staying attached as the flow proceeds along the flap and loses momentum with the radial surface still at a smaller radius. Although this shorter flap and larger θ was going to cause more pressure drag during cruise, the lift-augmentation it provides during takeoff and landing operations may prove more beneficial to the aircraft's performance

The second of the parameters that was investigated in this preliminary study on the dual radius configurations, was r_2 and the resulting ratio of r_2/r_1. Having small r_2 values, similar to r_1, was thought to result in increased flow turning angles, and while producing shorter flaps. Although, a shorter and steeper flap may encounter flow separation due to the slot flow not being able to follow the steep radial surfaces, the less drastic change in radii could help the flow stay attached. With r_2 values significantly larger than r_1, the flow would not have as much difficulty staying attached to the contour of the flap but may encounter issues with the larger discontinuity in the radii when r_1 changes to r_2. This larger r_2 would also not be as effective in turning the flow, by not being able to obtain high θ values.

The results of this preliminary study on dual radius flaps, being performed under a NASA research contract[9], provided insight into what additional flap parameters should be investigated to properly characterize the CC flap. This analysis was carried out using two-dimensional CFD and a k-ε turbulence model. The tested geometries, with specifications are presented blow in Figure 13. The study showed that the shorter dual radius flaps with larger θ values augmented greater lift, but the flaps with larger r_2/r_1 ratios had better L/D characteristics. Though the flaps with larger r_2/r_1 ratio produced an increase in L/D, as the length of the same flap is increased, the favorable L/D values quickly diminish.

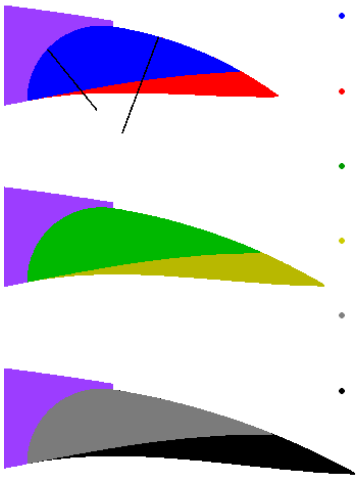

- Configuration C - $\left(\frac{r_2}{r_1}\right) = 5.13, \quad \left(\frac{c'}{c}\right) = 0.915$
- Configuration D - $\left(\frac{r_2}{r_1}\right) = 5.13, \quad \left(\frac{c'}{c}\right) = 0.94$
- Configuration J - $\left(\frac{r_2}{r_1}\right) = 8, \quad \left(\frac{c'}{c}\right) = 0.928$
- Configuration K - $\left(\frac{r_2}{r_1}\right) = 8, \quad \left(\frac{c'}{c}\right) = 0.97$
- Configuration N - $\left(\frac{r_2}{r_1}\right) = 10, \quad \left(\frac{c'}{c}\right) = 0.936$
- Configuration O - $\left(\frac{r_2}{r_1}\right) = 10, \quad \left(\frac{c'}{c}\right) = 0.99$

Figure 13. Previously studied CC dual radius flap configurations.

B. Geometry Study

Additional research was performed on the geometric parameters of the flap surface, given the preliminary results, to further characterize the flap shape. The next parameters that were examined were the shape, slope, slope rate of change, and curvature of the flap surface. The goal of this study was to analyze the geometric properties of the dual radius and develop alternative surface curves that would possibly offer enhanced aerodynamics.

The alternate curve that was compared to the constant radius curve of the dual radius flap was a prescribed radius curve. The prescribed radius curve takes on a specified radius given a position along the chord, similar to that of a spiral, which experiences self-preserving boundary layer characteristics along its surface[19]. This curves close characteristics to a spiral give it no instantaneous change in radius of curvature as the radius increases, unlike the dual radius flap surface. This prescribed radius curve matched the location, slope, and slope rate of change of the first constant radius curve of r_1 at the end of the curve. From there, it was chosen to have a cubic relationship with respect to the chord-wise direction of the airfoil. Allowing the radius to vary cubically, provided additional constraints that could be defined. One of these constraints is the control of the end radius of curvature of the surface, which was set to zero to assist in the flow leaving the trailing edge of the flap/airfoil with no angular component, increasing Kutta condition. On top of the constraints that were set by the first r_1 curve, the cubic-varying radius permits the end location and end radius of the curve. These design parameters define the next set of configurations to be analyzed.

For the analytic comparison of the two curves, a common dual radius shape[1, 2, 12, 13, 17, 20, 21], with a r_2/r_1 ratio of 5, was evaluated with a prescribed radius with a r_{2_avg}/r_1 of 30.7 and an end radius $60*r_1$. The results are presented below in Figure 14.

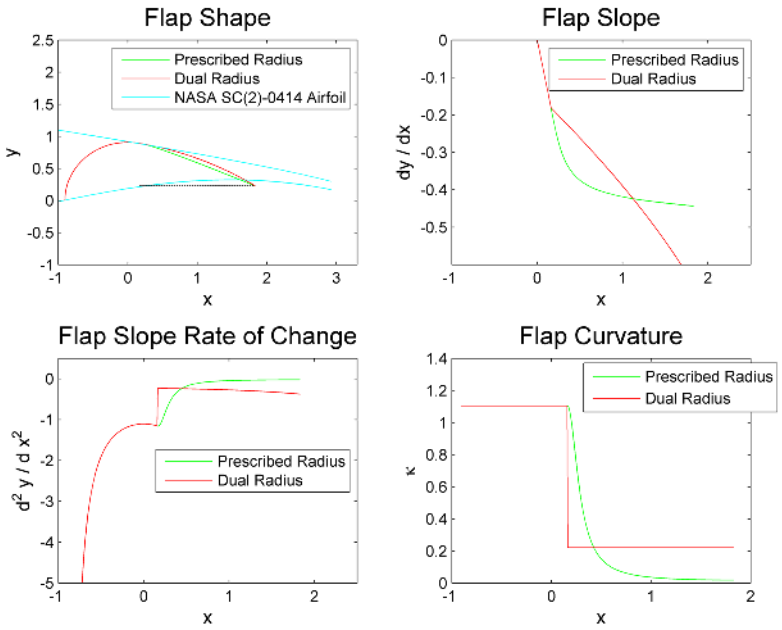

Figure 14. Flap surface analysis.

From the flap shape plot, the two curves appear very similar in physical appearance with the prescribed radius curve dipping slightly under the dual radius curve. Though, the rest of the four plots show the analytical difference between the curves. The flap slope plot shows the smooth transition from the r_1 curve to the secondary curve for the prescribed radius, where the dual radius has a non-smooth change in slope even though the flap slope is continuous. This can be seen further in the flap slope rate of change plot, where the dual radius has a discontinuity between r_1 and r_2. Although the prescribed radius curve experiences a steep slope after the r_1 curve on the curvature plot, it keeps a smooth slope transition between the two curves. Figure 15 displays a close up of the transition, where the smoothness can be seen more clearly on the prescribed radius curve. This smooth transition in curvature transitioning into a prescribed variation in radius, is believed to encourage flow attachment as the jet flow travels over the flap surface, thus being a central component in the following analysis.

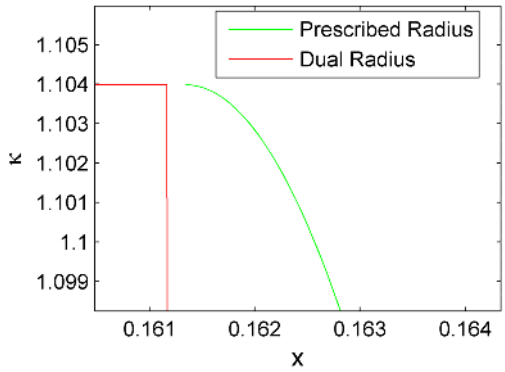

Figure 15. Curvature of flap surfaces.

Using analytical analysis of the curves, along with preliminary results, six geometries were created to further analyze and are presented in Figure 16 with specifications of each in Table 3. The callout names of each represent either dual radius (DR) or prescribed radius (PR), and the percentage of flap chord (c_f) of flap-modified chord (c'). The driving parameters of the dual radius flaps were r_2 and the length of the flap, where the prescribed radius flaps were driven by r_{2_avg} and length due to the cubic variation in radius. DR16 was the baseline dual radius configuration, being a common configuration of CC flap systems and having previous experimental[1, 2, 12, 13, 17, 20] and numerical data available[20, 21]. PR16 was base on the same length as DR16, with the smooth slope and curvature transitions accomplished by the prescribed radius. DR22 and PR22 were created by extending the length of the flap and increasing r_2 or r_{2_avg} to have the upper surface of the flap to closely math the top of the original airfoil. This

effort was made to keep the flap-modified airfoil as close as possible to the original airfoil's shape. DR19 and PR19 where then developed to add an intermediate flap between the -16 and -22 series, resulting in a length and radius in between the two. All flap configurations will be analyzed at a 60° flap deflection, due to the lift augmentation encountered with moderate drag penalties to follow. This will be an adequate representation of flap setting used for takeoff or approach.

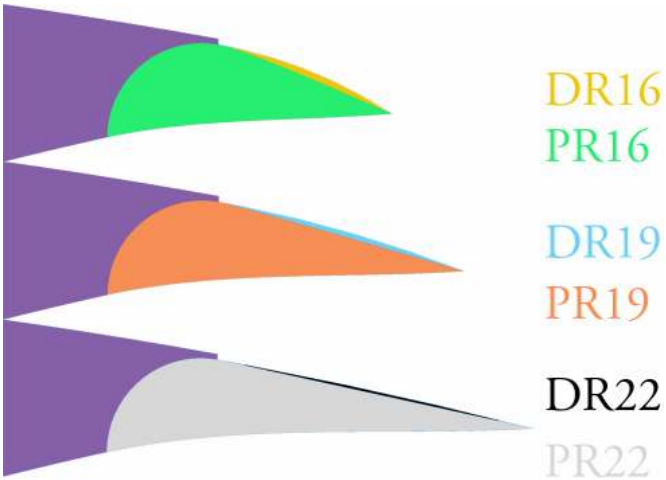

Figure 16. Flap configurations.

Table 3. Flap configuration specifications.

Configuration	c'/c	c_f/c'	(r_2 or r_{2_avg}) /r_1	θ
DR16	0.9414	0.1558	5	33.12°
PR16	0.9414	0.1558	30.7	23.92°
DR19	0.9782	0.1875	14.14	21.22°
PR19	0.9782	0.1875	291.5	16.18°
DR22	1.015	0.2169	48	14.36°
PR22	1.015	0.2170	3721	12.35°

IV. Numerical Simulation

A. Grid Generation

To accurately capture the complex flow physics of circulation control, a semi-structured mesh was utilized. The different regions that were created across the domain comprised of a structured exterior, an unstructured interior region, and a structured slot, boundary layer, and wake region. Figure 17 below displays the entire domain. This figure shows the details of the structured exterior region which promote cell orientation in the freestream direction, helping in reducing the time for the solver to compute the governing equations. The exterior region extends five chord-lengths above and forward of the airfoil, ten chord-lengths downward, and 15 chord-lengths aft. This large domain ensured that the flow physics of the CC airfoil were captured.

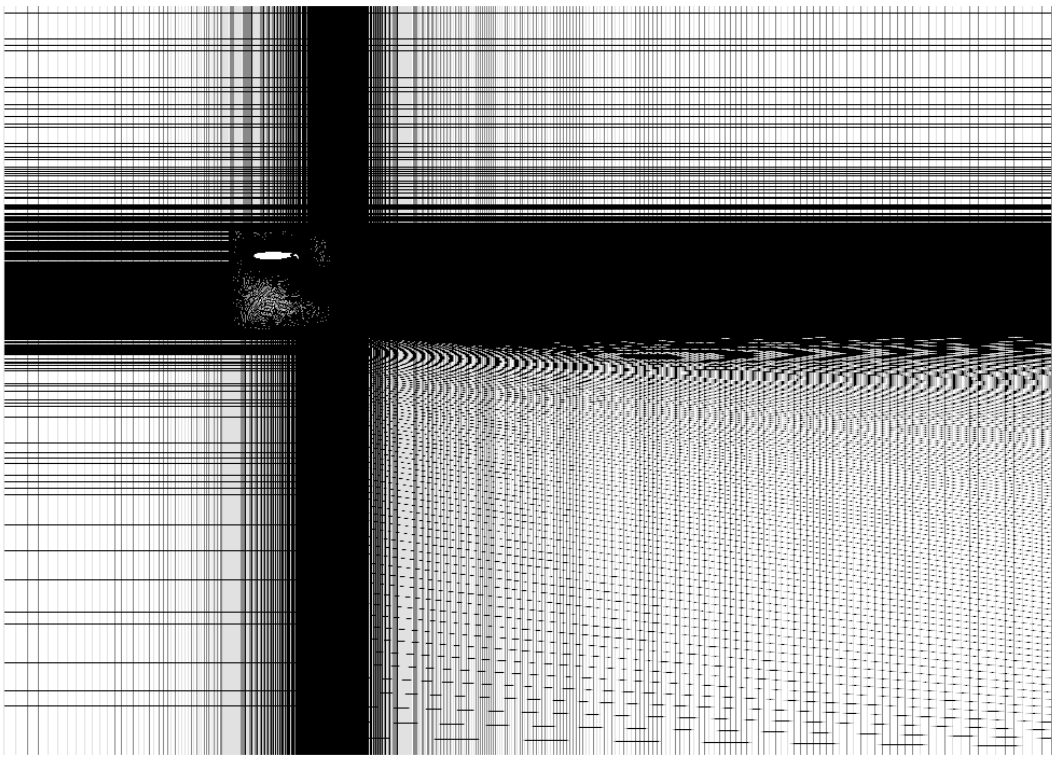

Figure 17. Entire computational domain.

The interior region was left unstructured to help in the transition from the structured grid of the curved airfoil and flap to the structured grid of the orthogonal exterior region. The unstructured grid also allowed for a more rapid growth in cells in regions that did not need the refinement. This interior region was extended a half of a chord-length forward and above the airfoil and a chord-length and a half below and aft of the airfoil. Figure 18 below depicts this interior region.

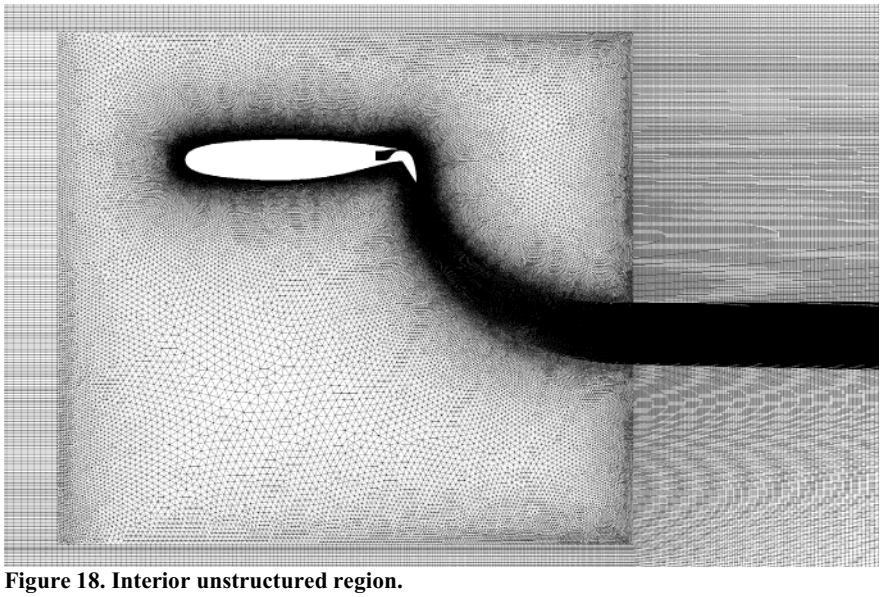

Figure 18. Interior unstructured region.

Using the CAD program, Pro/ENGINEER Wildfire 4.0, the boundary layer, slot, and wake regions were created and broken into segments. Figure 19 shows how these different regions and segments were created. Figure 20 displays the computational grid of these segments and how the unstructured interior grows from the structured segments.

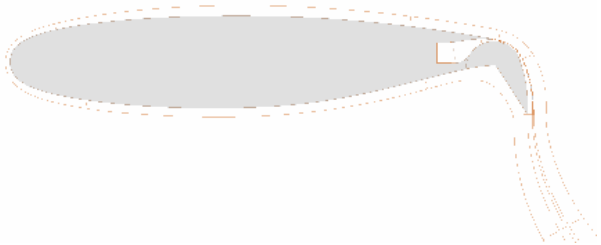

Figure 19. Different segments of structured grid.

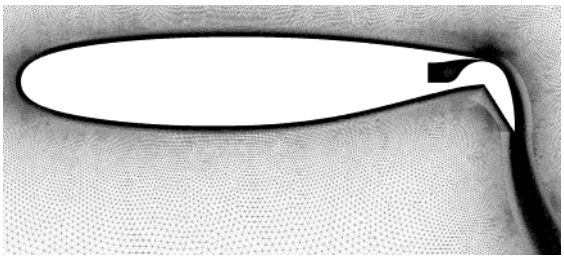

Figure 20. Computational grid of airfoil.

A structured grid was used in the boundary layer to ensure orientation in the flow direction and to keep from cell skewness in this region. The first slot height of the boundary layer was specified to aim for a y+ value of 1 or lower to keep high accuracy of the solution. The structured segments of the boundary layer, slot, and wake flow regions started on the airfoil or plenum and travel all the way through the domain out the exit of the exterior, to capture the high property gradients of these regions. Figure 21 presents the details of the slot region with the various different structured segments. This figure also details the growth of the boundary layer region into the transition of the unstructured interior.

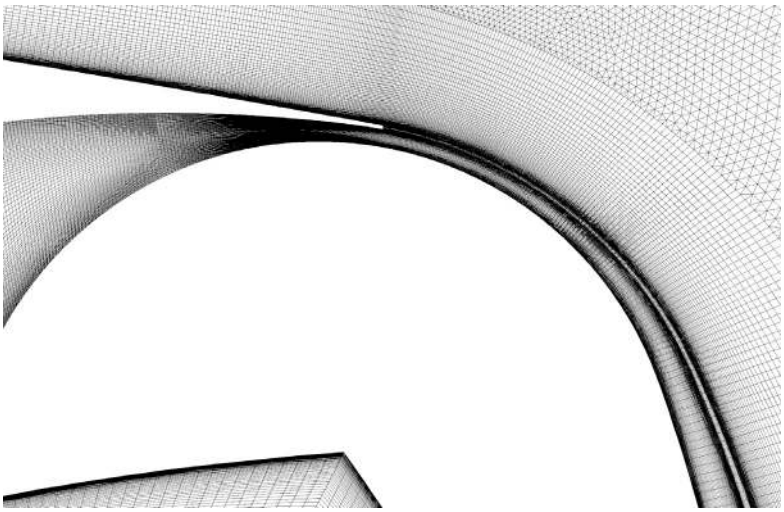

Figure 21. Details of the slot region.

B. Solver Settings

The solver used for the simulation was Fluent 6.3. A pressure far-field was the boundary type assigned to the inlet, outlet, and symmetry planes. The airfoil and plenum wall were treated as walls, with the plenum inlet getting assigned a pressure inlet boundary type. The solver was set to implicit and density-based. The turbulence model selected for this simulation was the realizable k-ε[22] with no near-wall treatment due to the grid refinement. This model was chosen over the Spalart-Allmaras[23] and k-ω[24] models because of its ability to capture turbulence features with a high quality near-wall mesh, and being commonly used and robust[25]. Table 4 below displays the rest of the solver settings that were used for the following analysis in Fluent.

Table 4. Fluent 6.3 solver settings.

Solver	Density-Based/Compressible
Turbulence Model	Realizable k-ε
Near-Wall Treatment	None
Density Calculator	Ideal-Gas Law
Viscosity Calculator	Sutherland's Law
Domain Boundary Type	Pressure Far-Field
Plenum Inlet Boundary Type	Pressure Inlet

C. Boundary Conditions

The boundary conditions were set to achieve a moderate momentum coefficient (C_μ) and the low-speed airspeed encountered during takeoff, landing, and approach. The target 2-D C_μ was 3, and was calculated using

$$C_\mu = \frac{\dot{m}_{slot} * V_{slot}}{q_\infty * c} \tag{1}$$

where $\dot{m}_{slot}$ is the 2-D slot mass flow rate calculated with only the slot height. The goal of the slot flow was to stay below sonic. This would add less complexity to the plenum and slot design, not having to devise a converging-diverging nozzle which was also impractical for the AMELIA wind tunnel model by the noise implementations sonic flow would impose on the N+2 goals. Though it should be noted that above sonic flow has been seen to not have negative effects on the Coanda flow of CC, but yield additional lift gains[6, 8]. To ensure sonic flow was not achieved, the critical area of the slot was computed using

$$\frac{A}{A^*} = \frac{1}{M} * \left[\left(\frac{2}{\gamma+1} \right) * \left(1 + \frac{\gamma-1}{2} * M^2 \right)^{\frac{\gamma+1}{2*(\gamma-1)}} \right] \tag{2}$$

With this equation, the design geometry, and sea level static conditions, a plot of C_μ vs. M_∞ was constructed with a sonic slot limit line to visualize the design area. This graph is presented in Figure 22 below, with the chosen design point which represents a freestream Mach of 0.1 or 66 knots.

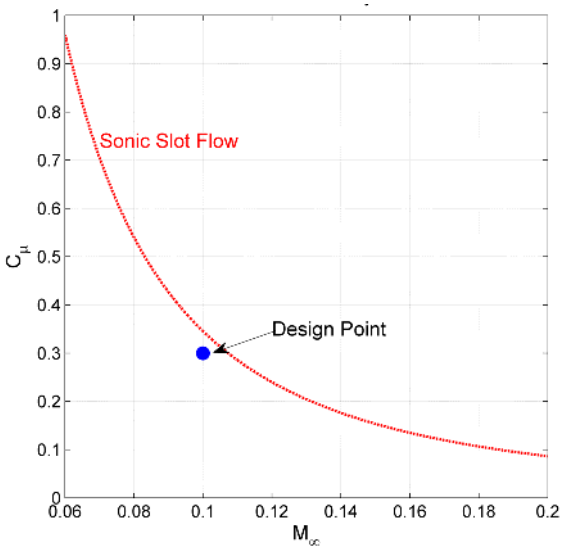

Figure 22. Maximum C_μ attainable.

From the chosen M_∞, sea level static conditions, and Equation 1, the slot boundary conditions were computed. To do this, the 2-D mass low rate had to be derived from the mass flow definition and Equation 1. The resulting equation follows

$$\dot{m}_{slot} = \sqrt{\frac{C_\mu * P_{slot} * h_{slot} * q_\infty * c}{R_\infty * T_\infty}} \tag{3}$$

where P_{slot} represents the static pressure at the exit of the slot, which has been measured from previous analysis of the geometry, and $\dot{m}_{slot}$ represents the 2-D mass flow rate per span. From Equation 3 and Equation 1, V_{slot} and M_{slot} can be backed out. This is then used to find the stagnation pressure and temperature at the slot assuming freestream static temperature at the slot exit and with the following equations

$$P_{stag} = P_{slot} * \left(1 + \frac{\gamma - 1}{2} * M^2\right)^{\frac{\gamma}{(\gamma - 1)}} \tag{4}$$

$$T_{stag} = T_{slot} * \left(1 + \frac{\gamma - 1}{2} * M^2\right) \tag{5}$$

Table 5 below presents all of the boundary conditions that were used in Fluent for the simulation.

Table 5. Boundary conditions.

Freestream Conditions		**Slot Conditions**	
M_∞	0.1	M	0.8128
ρ_∞ (kg/m^3)	1.225	h_{slot} (m)	$1.127406*10^{-3}$
T_∞ (K)	288.15	P_{stag} (Pa)	148,220
P_∞ (Pa)	101,325	T_{stag} (K)	326.2
μ_∞ (kg/(m*sec))	$1.81205*10^{-5}$	C_μ	0.3
R_∞ (J/(kg*K))	287.058	δ_f (°)	60
q_∞ (kg/(m*sec^2))	709.29		

V. Results

The six different flap configurations were analyzed at three different α's for the same freestream and C_μ values. The objective of this analysis was to characterize the geometric parameters of these different CC flap configurations to better understand the resulting flow features and performance of each. C_l, C_d, $C_{m,(c/4)}$, C_p, and C_f were measured for each of the configurations to determine their performance, along with plots of Mach contours and streamlines to help visualize the flow physics occurring around the airfoil. Table 6, on the next page, presents the results for all six of the different flap configurations for the $\alpha = 0°$ cases. For visual results of the configurations at all of the α's tested, refer to the Appendix.

Table 6. Streamlines and contours of Mach at α = 0°.

c_f/c'	Dual Radius	Prescribed Radius
16%	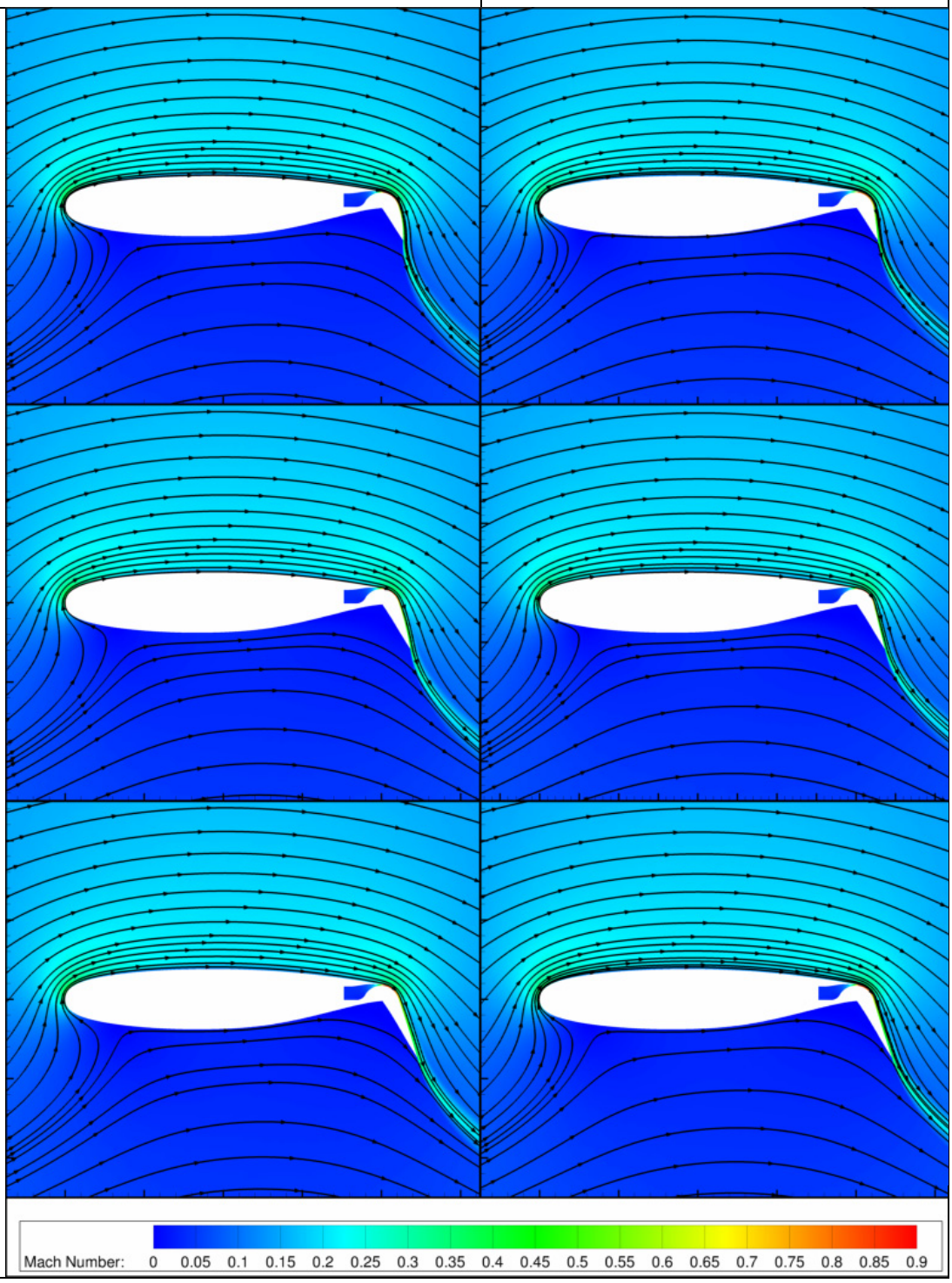	
19%		
22%		

Several points can be taken from the flow visualization of the simulation, presented in Table 6. The first being the difference in stagnation point location, not only for the different length in flaps but also the dual radius versus the prescribed radius configurations. The location of the stagnation points for the different configurations point toward the effect each have on their ability to augment forces. For the dual radius configurations, the lengthening of the flap brings the stagnation point further forward on the lower surface of the airfoil. This is not quite the case for the prescribed radius flaps, with PR16 and PR22 having similar stagnation point locations and PR19 experiencing a further aft location. When comparing the 16% dual radius to the prescribed radius, the prescribed radius encounters a significantly forward stagnation point location. Though when observing the 19% and 22% flaps, this occurrence does not appear as noticeable. Looking at the aft region of the flow visualization, it is noted that the longer flaps with smaller θ allow the aft streamlines to smoothly transition over the trailing edge of the flap surface rather than experience the much more abrupt and rapid turns of the shorter flaps. Again, this shows the flaps effectiveness on force augmentation, but more specifically drag and moment augmentation.

The analytical plots of C_l vs. α and C_d vs. α displayed in Figure 23 and Figure 24, respectively.

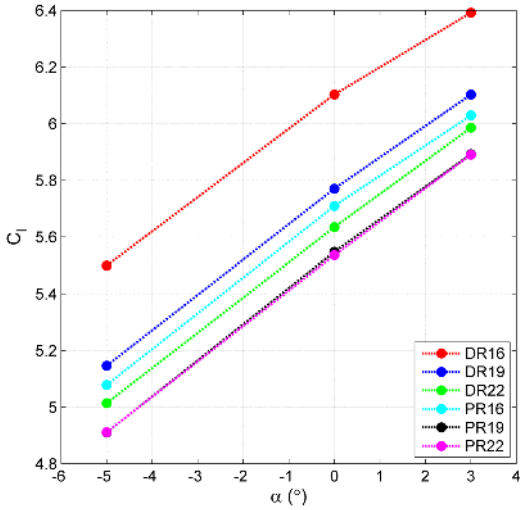

Figure 23. Lift curve for different flap configurations.

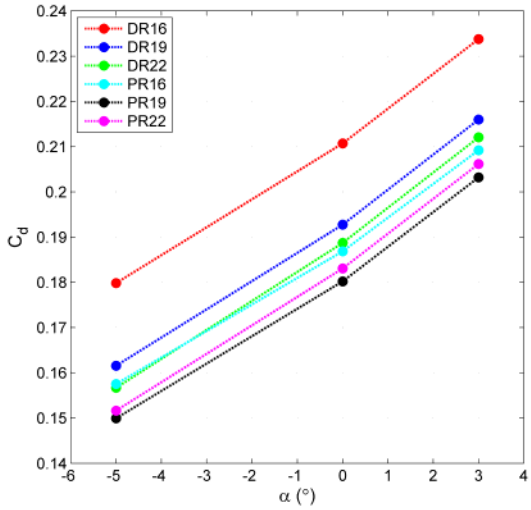

Figure 24. Drag coefficient as a function of α.

From Figure 23 above, it is evident that configuration DR16 achieves the greatest lift augmentation, reaching a 2-D C_l of 6.4 at α = 3°. The lift curve for DR19 drops off significantly from DR16, having a 5.5% average drop in lift. The reason for this significant variation in lift between DR16 and the other flaps can be attributed to the larger departure angle (θ) encountered on DR16 with the smallest flap exit radius. DR19 slightly outperforms PR16, having only a 1.2% average increase in lift. Though this increase in lift of DR19 over PR16 cannot be attributed to θ, due to PR16 having a slightly larger θ of 23.92° compared to the 21.22° of DR19. Instead these additional lift gains can be ascribed to the 3% increase in flap length. Configurations PR19 and PR22 perform very similarly, having about the same lift curve and being an average of 2.8% below the PR16 lift curve and 1.7% below the DR22 curve. The similar lift-performance of PR19 and PR22 could be due to the additional 3% length of flap in the PR22 making up for the smaller θ angle of PR22 and yielding about the same lift.

Observing the drag values from Figure 24 revels that configuration PR19 has the lowest average drag of about 0.1778 throughout the three α's. PR22 has a slight increase in average drag for the α-sweep of 1.38% over PR22, having the second lowest drag curve. PR16 and DR22 have very similar drag values for α = -5°, but then the drag for DR22 increases throughout α = 0° and 3°. Similar to the PR-series, the average drag values increase 2.31% from the 22% to the 19% dual radius configurations. DR16 exhibits the largest drag values by far, with an average C_d value of 0.2081. This can be tied to the significantly larger lift augmentation achieved by this configuration. All of the prescribed radius configurations outperform the dual radius configurations in drag-performance. This is partly due to the additional lift values attained by most of the dual radius configurations over the prescribed radius flaps, except for DR22 and PR16. In this instance the lift of PR16 surpasses that of DR22, along with keeping lower drag values. Looking back at the specifications of each of the flaps, this shows that low drag values can be achieved with high θ values even though the r_2/r_1 ratio of DR22 (48) is greater than the r_{2_avg}/r_1 value of PR16 (30.7). This contradicts what was found in the preliminary studies preformed on the various dual radius configurations, but can

be attributed to the different geometrical shape of the prescribed radius configurations. Through the observations of lower C_d values experienced by the prescribed radius configurations over the dual radius configurations, the drag benefits of the prescribed point to their smoother transitions in slope and curvature, on-average lower θ, and lower end curvature.

To directly compare the C_l and C_d values with each other and α, the plots of C_d vs. C_l and L/D vs. α were constructed and presented below in Figure 25 and Figure 26.

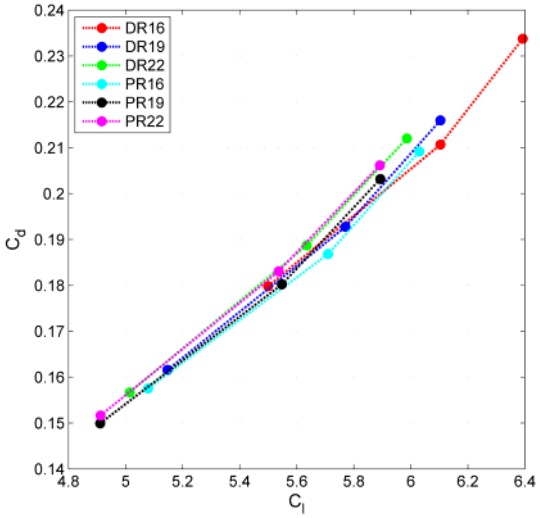

Figure 25. Drag polar for flap configurations.

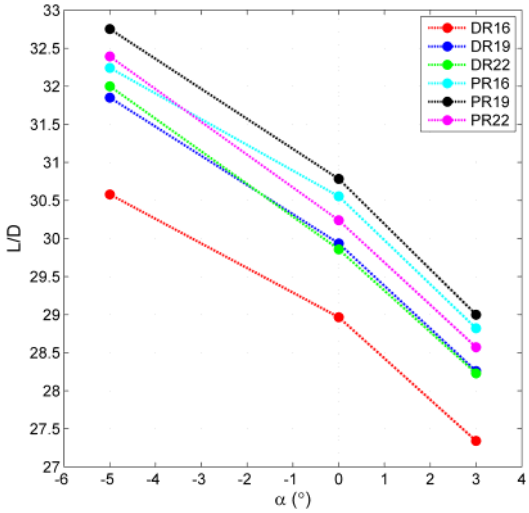

Figure 26. Lift-to-drag ratio as a function of α.

From the C_d vs. C_l plot above, it can be seen that all of the CC flap configurations have very similar drag values given lift. DR16 curve still extends significantly further than the rest, due to the large amount of lift augmentation created. The top two curves of this plot are the 22% flaps, with PR22 just exceeding the DR22 configuration. The bottom two curves of this plot are both of the 16% flaps, with PR16 the lowest for low C_l then transitions to DR16 once the C_l values exceed 5.9.

The L/D vs. α plot above provides more insight between the lift and drag numbers of the analysis. This plot clearly highlights PR19 with the highest L/D ratio over the other configurations, reaching up to an L/D of 32.8 at α = -5° and average L/D of 30.8. The next two best performers of L/D ratio are the other two prescribed radius configurations, with PR16 having an average L/D of 30.5 and PR22 with average L/D of 30.4. The next two curves represent DR19 and DR22 both with average L/D values of 30.0. DR16 falls an average of 3.5% below the two other dual radius configurations. The trends presented by this plot clearly shows better L/D performance out of all the prescribed radius configurations, with PR19 performing the best. Looking at both dual radius and prescribed radius L/D performance, the intermediate 22% flaps obtain the best L/D values. This suggests that the best configuration for high L/D being one with a prescribed radius with intermediate flap length and θ of about 16°.

Figure 27 and Figure 28 display the $C_{m,(c/4)}$ data for the six different configurations below.

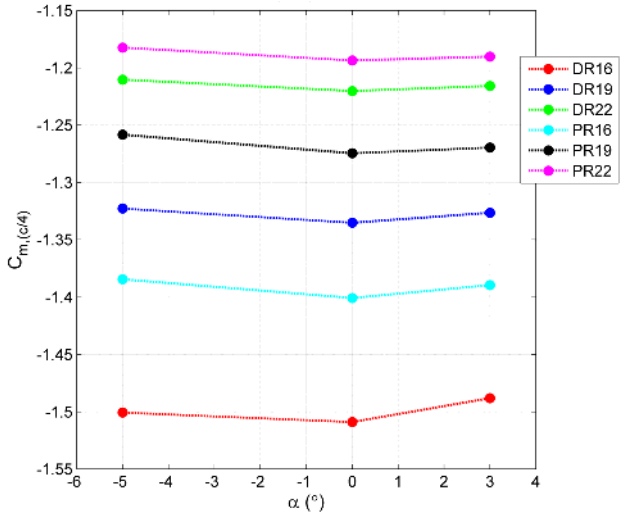

Figure 27. Quarter-chord moment given α.

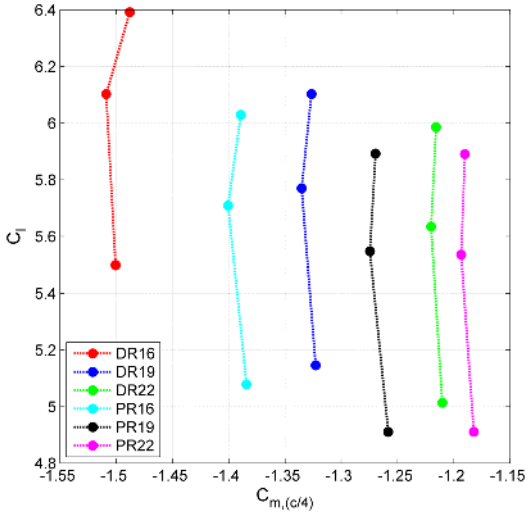

Figure 28. Lift for a given quarter-chord moment.

The $C_{m,(c/4)}$ plots show the large negative moments encountered by the use of CC flap systems, which has been seen in past research[1, 2, 4, 12, 13, 17, 18]. DR16 experiences the worst negative $C_{m,(c/4)}$ of -1.5, which can be directly attributed to its large lift augmentation. Following DR16 is PR16 with a 7.2% decrease in negative moment. Looking at dual radius and prescribed radius results separately, they experience a similar relationship with the length of the flap and the magnitude of the negative quarter-chord moment with the longest flaps encountering the least moment. The C_l vs. $C_{m,(c/4)}$ plot above helps visualize what negative moment has to be taken for a given lift value. This shows that the DR16 configuration obtains the highest lift, but with highest moment to follow. DR19 obtains the next highest lift with a 5.5% average decrease in lift and an 11.4% decrease in quarter-chord moment. These plots clearly show that flap length directly influences the negative moment encountered.

More detailed analysis of the different configurations can be observed through the C_p vs. x/c' plot for the $\alpha = 0°$ cases, displayed below in Figure 29 with the red vertical line representing the slot location.

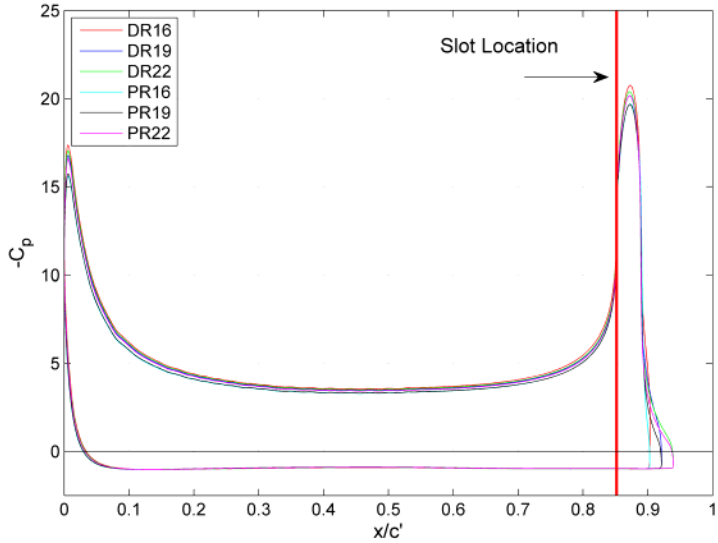

Figure 29. C_p distribution on the airfoil.

From the C_p plot above, all configurations experience similar pressure distributions over the airfoil with a large suction peak near the leading edge and even bigger peak occurring over the blown flap surface. This larger pressure peak of the aft part of the airfoil is caused by the CC blowing performed on the trailing edge of the airfoil and gives the airfoils the large associated negative pitching moment. It is evident that the configurations vary the most on the suction peaks, as well as the longer flaps extending further in the x-direction. Another observation, would be the sudden drop in C_p, or sudden flow deceleration, around x/c' of 0.89. This location corresponds with the change in flap surface, from the constant arc r_1 to the secondary flap surface determined by each flap configuration. All of the configurations experience this adverse pressure gradient, which could be problematic in causing upper surface separation for lower C_μ cases. To examine the variations in suction peaks between the configurations, a zoomed in view of both leading edge and trailing edge peaks are pictured below in Figure 30 and Figure 31.

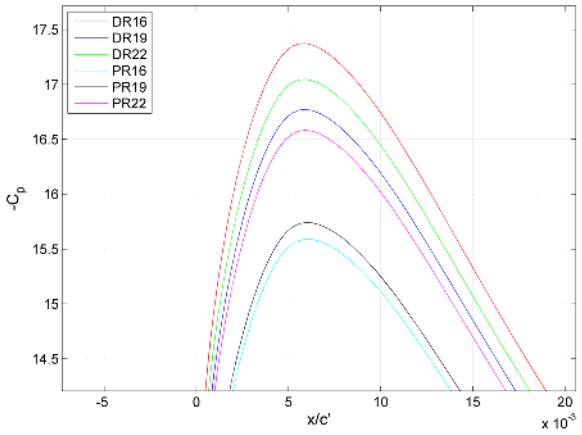

Figure 30. Leading edge suction peak.

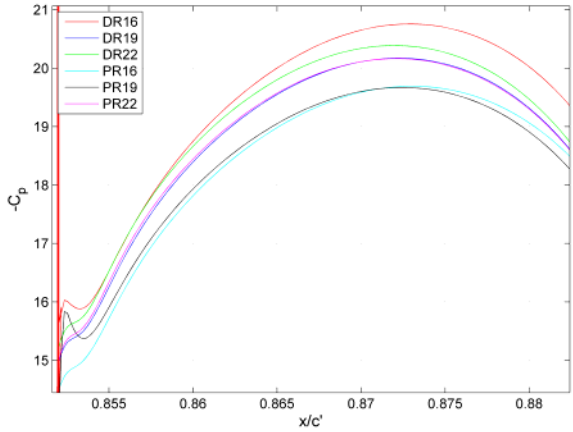

Figure 31. Trailing edge suction peak.

The leading edge suction peak plot displays all three dual radius configurations superior in obtaining a more negative pressure peak, with DR16 below the rest at -17.4 and DR22 following at -17.1. PR22 generates the most negative pressure peak of the prescribed radius flaps at -16.6, falling just shy of the peak of DR19 at -16.8. Figure 31 displays very similar trends of the different configurations on the trailing edge suction peak, with DR16 and DR22 achieving more negative pressure peaks (-20.8 and -20.4) than any of the prescribed radius flaps, and DR19 having about the same pressure peak as the best performing prescribed radius configuration of PR22 at -20.2. These pressure plots reveal the dual radius configuration attains more negative pressure peaks than the prescribed radius flaps. There is a small deceleration in the flow directly aft of the slot, shown by the slight decrease in slope of C_p just aft of the red, slot location line in Figure 31. The source of this is believed to be the small recirculation region near the slot, caused by the small gap between the slot opening and the upper surface of the airfoil. This occurrence is depicted in Figure 32 below.

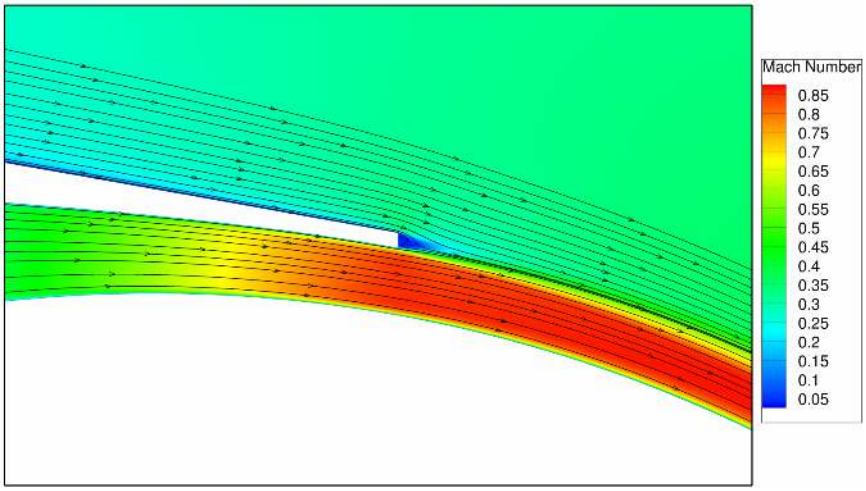

Figure 32. Recirculation caused by material gap between slot and airfoil upper surface.

Figure 33, below, features the C_p values acting directly on the flap surface. This clearly shows that all three dual radius flaps carry a more negative C_p further aft on the flap surface when compared to the prescribed radius flaps. This is the cause of the dual radius encountering larger negative pitch down moments when compared to the same length prescribed radius configuration.

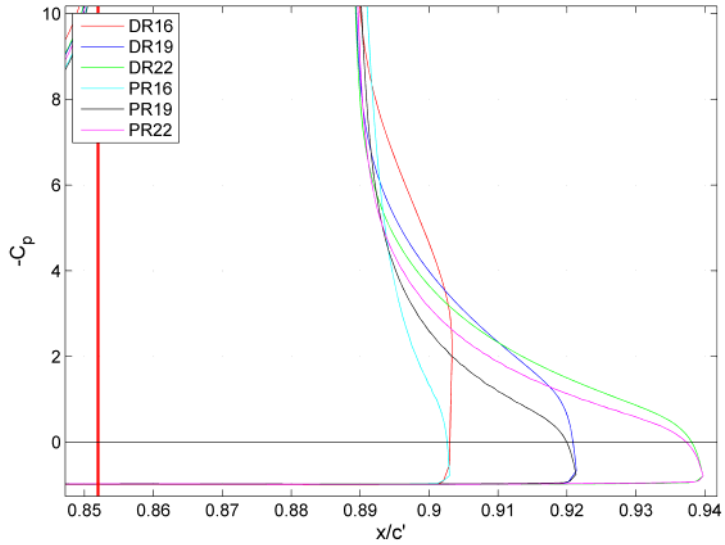

Figure 33. Pressure distribution over each flap.

C_f was then computed on the surface of each of the airfoils for analysis, which is shown in Figure 34 below.

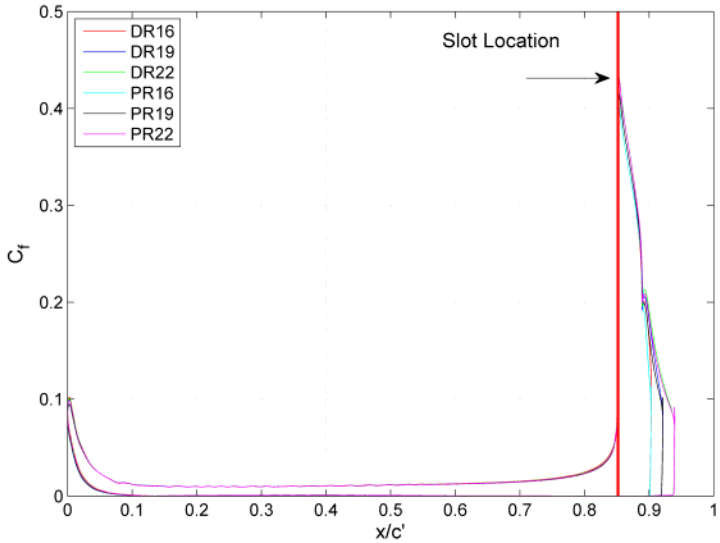

Figure 34. Skin friction coefficient on airfoil surface.

This plot provides the general skin friction encountered during CC operation, with slot location given with vertical red line. Forward of the slot, all of the configurations behave very similar, with the leading edge peaks vary slightly between the configurations, occurring in the same order as the C_p plots above. It is evident that the main variation of C_f takes place aft of the slot, where the influences of the geometry of each of the configurations come into play. Figure 35 below details C_f numbers in the region aft of the slot which is where the surface of each configuration varies.

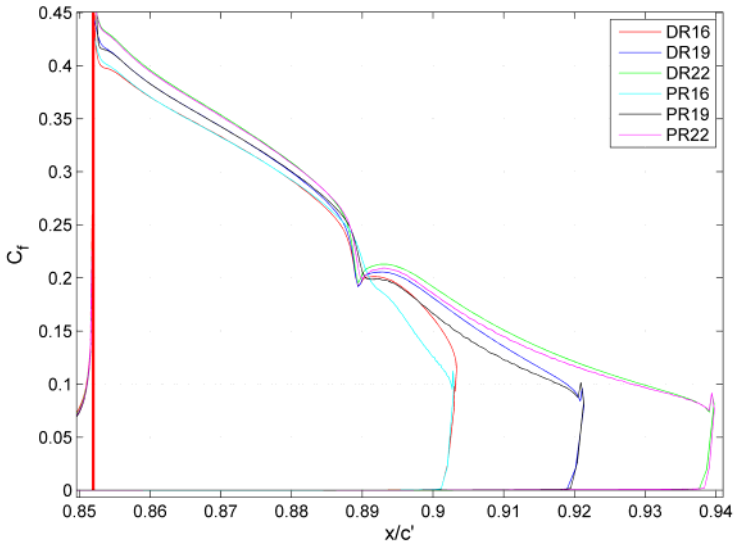

Figure 35. Skin friction distribution on flap.

All of the configurations have a small decrease in C_f shortly aft of the slot, which is again attributed to the small amount of recirculation caused by the material gap between the slot opening and the upper surface of the wing (Figure 32). When inspecting this aft region of the airfoil, it can be seen that the length of each of the flaps has the most effect on the C_f value. The longer the flap length, the larger the C_f value for the duration of the flap. When comparing the same length dual radius and prescribed radius flaps follow about the same C_f along the flap until they encounter a pronounced drop-off and recovery at about a x/c' of 0.89. After this "dip" in C_f the dual radius configurations' skin friction rises back up slightly, where the corresponding length prescribed radius flaps remain at this decreased skin friction slope for the shorter flaps and only slightly rebound for the longer prescribed radius flaps. This gives more insight into why the dual radius configurations experience more drag than the corresponding prescribed radius flaps, though might be favorable in keeping the flow attached to the flap surface during extreme deflections or low values of C_μ. This C_f "dip" is explored in greater depth below in Figure 36.

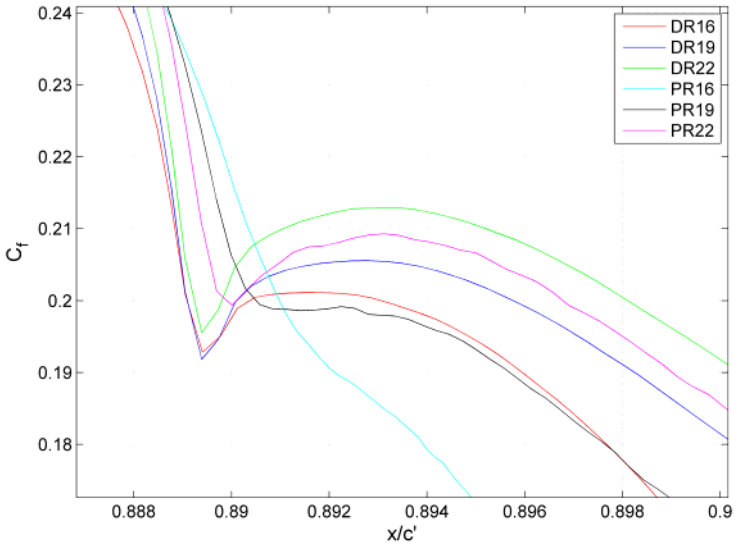

Figure 36. Detailed view of flap surface transition.

By examination of the above plot and the geometry of the different flap configurations, it can be noted that this "dip" signifies a large decrease in speed and takes place at the location where each flap transitions from r_1 into either r_2 for the dual radius or into the cubically varying radius of the prescribed radius flap. The effect of this curvature change on the skin friction can be seen by the severity of the "dip" encountered by each flap. When tracking the influence of the flap length on the skin friction it appears that the longer the flap, the greater the rebound in C_f values after the sharp decrease. Comparing the prescribed radius flaps to the dual radius flaps, it is evident that the

prescribed variation in radius, greatly smoothes the sharp fluctuation in skin friction, with PR16 enduring the smoothest change in the skin friction slope and PR22, having the sharpest change. This is characterized by how quickly each of the prescribed radius flap curvatures departs from the curvature of the r_1 arc on the flap. This concept is visualized in Figure 37 below.

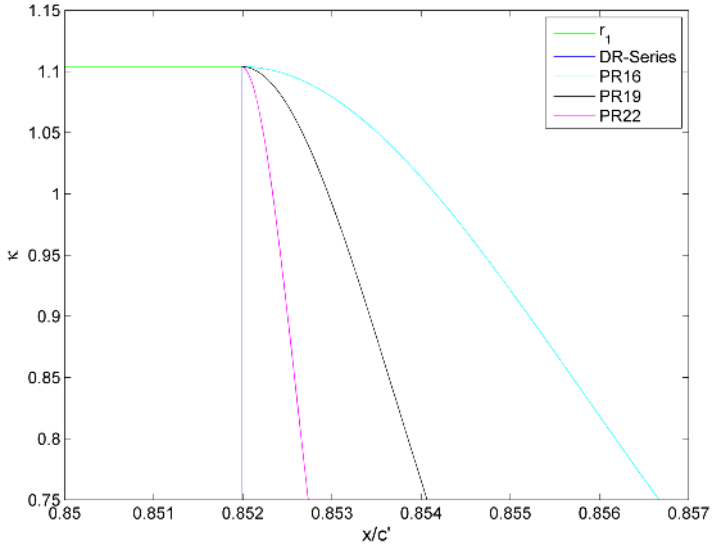

Figure 37. Departing curvature of the prescribed radius flaps.

When comparing the flap characteristics presented on the above plot to Figure 36, the effect of the departing curvature of each flap is more clearly observed. The more severe "dip" in PR22 is due to its curvature quickly departing from the original curvature of r_1. This also shows how the smooth and gradual curvature changes of PR16 are beneficial in keeping the flow over the top of the flap surface attached through large flap deflections for lower cases of C_μ. Another point is that the rapid change in C_f also coincides with the large pressure increase in the C_p plots, defining a rapid deceleration of flow. This proposes that the more rapid changes in curvature directly influence adverse pressure gradients, which could cause separation at lower values of C_μ or larger flap deflections. This influence of flap curvature could provide an example of the onset of the "super-circulation control" observed by past research[2, 26, 27].

Figure 38, below, presents the wall y+ values encountered during the simulation.

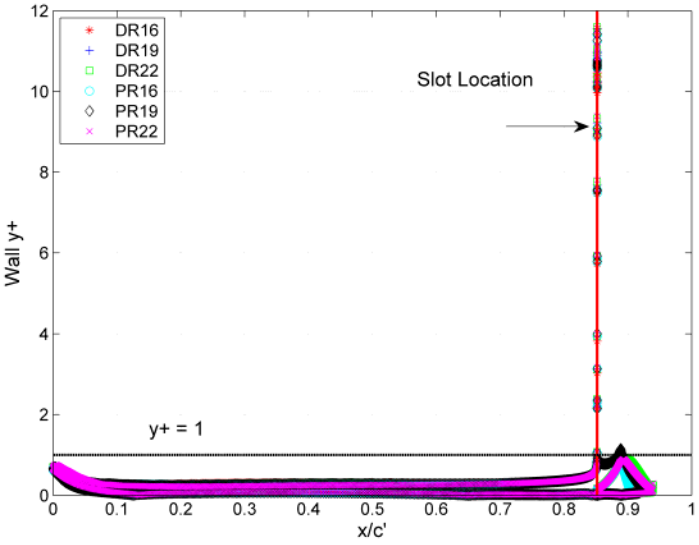

Figure 38. y+ values of the different flap configurations.

The y+ values for all of the different flap configurations stay at one or below, except for the slot location. The same problem was encountered by Lee-Rausch[20], who reduced spacing by a factor of four to see little difference in solution. Reduction of the cell height at the slot would significantly drive up cell count, greatly increasing solving time. For these reasons, the current y+ values deemed adequate.

VI. Conclusions

By exploring the design space of various CC flap systems, several performance characteristics were developed which provide insight into the geometrical effects of the CC flap. The parameters varied in this study showed that the largest lift augmentation was achieved with the shorter, dual radius flap that keeps a large curvature throughout the exit of the flap and a large θ value. Although very large negative pitching moments are associated with such lift augmentation, along with large drag penalties resulting in the lowest L/D values of all of the flap configurations. This could yield negative impacts on the design of the system implementing such a flap configuration, requiring additional thrust and control surface area. In terms of the lowest adverse moments encountered, the longer the flaps experienced less negative moment with the prescribed radius geometry performing better by not carrying as much negative pressure over the blown flap surface as the comparable dual radius flap.

Although the prescribed radius configuration developed in the paper does not match the same lift augmentation as the dual radius flaps, it outperformed the dual radius in several other categories. Those being the drag induced by the flap, higher achievable L/D ratios, lower negative moments, and a more favorable curvature promoting flow attachment for lower values of C_μ. The skin friction measurements revealed the importance of a smooth and gradual change in curvature by developing sudden gradients along the flap surface where the curvature changed instantaneously or rapidly, where flaps with this steady transition encountered a slower change in C_f. This research provides insight into the arena of CC flap design in order to improve existing CC flaps, along with aid in the development of new better performing systems.

VII. Future Work

The same set of flap configurations is set to be simulated with 90° flap deflection to observe the characteristics at a larger flap deflection. This data will provide further insight into the geometrical effects of the flap at a more extreme case. A cruise configuration of the six flap configurations is also set out for analysis to measure the airfoil performance when the flaps are at 0° deflection and speeds are reaching super-critical.

Throughout further research into the curvature parameter of the CC flap, an additional assortment of prescribed radius flaps are well within reach of being developed and could greatly enhance the performance flap system. With control over the prescribed variation of the flap radius, the flap can be altered to achieve a specific desired performance. This area of CC studies is not thoroughly researched, and could hold some interesting results.

Further work will be performed on the k-ε turbulence model, since it has been shown to over predict lift significantly[28] due to the assumptions it takes on[29]. This is caused by the over predicting of the turbulent kinetic energy production[30] and failure for the model to follow streamline turning during CC flows[26]. This makes the k-ε turbulence model inadequate for capturing separation or recirculation regions. A parallel effort is underway to improve the CFD modeling of CC configurations with the development of an improved turbulence model for CFD that will predict the increased circulation flow field of the CC flap much more accurately[31]. This model will be a v^2-f extension of the k-ε model which will account for non-local wall effects, nonlinear eddy viscosity, and curvature corrections. Preliminary case studies of this model show results almost matching experimental data exactly, where the k-ε and k-ω models over-predict C_l significantly. The linear and nonlinear v^2-f extension of the k-ε model is currently being validated with more basic predictions, before used for CC flap analysis. Though the extent of this research was to observe the performance characteristics of the different geometrical flap parameters, rather then validation of experimental data or simulating stall where these problems would degrade the solution.

VIII. Acknowledgements

The authors would like to acknowledge the NASA Research Announcement award under Contract #NNL07AA55C, with technical monitors Craig Hange and Clif Horne, which provided funding for this work. The authors wish to thank the hard work of Jay Marcos and the rest of the researchers at Cal Poly, who provided valuable effort in obtaining the preliminary and final results.

References

[1]Englar, R. J., Smith, M. J., Kelley, S. M., Rover III, R. C., "Application of Circulation Control to Advanced Subsonic Transport Aircraft, Part 1: Airfoil Development," Journal of Aircraft, Vol. 31, No. 5, Sept.-Oct. 1994.

[2]Englar, R. J., "Overview of Circulation Control Pneumatic Aerodynamics: Blown Force and Moment Augmentation and Modification as Applied Primarily to Fixed-Wing Aircraft," NASA/CP-2005-213509/PTI, June 2005.

[3]Wood, N., and Nielson, J. "Circulation Control Airfoils Past, Present, and Future," AIAA Paper 850204, January, 1985.

[4]de la Montanya, J., "Circulation Control: Past to Present," NASA/Cal Poly ESTOL Project Team, September 2005.

[5]Chang, P. A. III, Slomski, J., Marino, T., Ebert, M. P., Abramson, J., "Full-Reynolds Stress Modeling of Circulation Control Airfoils," Naval Surface Warfare Center - Carderock Division, West Bethesda, MD, March 2004.

[6]Englar, R. J., "Experimental Investigation of the High Velocity Coanda Wall Jet Applied to Bluff Trailing Edge Circulation Control Airfoils," Naval Ship R&D Center (NSRDC) Rept. 4708, Aero Rept. 1213, AD-A-019-417, Bethesda, MD, Sept. 1975.

[7]Englar, R. J., "Subsonic Wind Tunnel Investigation of the High Lift Capability of a Circulation Control Wing on a 1/5 Scale T-2C Aircraft Model," NSRDC Report ASED-299, AD A7781856, May 1973.

[8]Englar, R. J., "Investigation into Application of the High Velocity Circulation Control Wall Jet for High Lift and Drag Generation on STOL Aircraft," AIAA Paper 74-502, November 1976.

[9]California Polytechnic State University San Luis Obispo, Georgia Tech Research Institute, DHC Engineering, "The Integrated Modeling and Verification of a Hybrid Wing-Body Low Noise ESTOL Aircraft," NASA Contract #NNL07AA55C, Oct. 2008.

[10]Rich, P., McKinley, R. J., Jones, G. S., "Circulation Control in NASA's Vehicle Systems," NASA CP-205-213509 (part 1), June 2005.

[11]Loth, J. L., "Some Aspects of STOL Aircraft Aerodynamics," AIAA Paper 83-0082, April 1973.

[12]Englar, R. J., Trobaugh, L. A., Hemmerly, R. A., "STOL Potential of the Circulation Control Wing for High-Performance Aircraft," David W. Taylor Naval Ship Research and Development Center, Bethesda, MD, March 1978.

[13]Englar, R. J., "Application of Advanced Aerodynamic Technology to Ground and Sport Vehicles," AAIA 2008-6731, Georgia Tech Research Institute, Georgia Institue of Technology, Atlanta, GA, August, 2008.

[14]Englar, R. J., "Final Report: Summary of Research: Continued Development and Application of Circulation Control Pneumatic Technology to Advanced Transport Aircraft," NASA/CR-1998-207471.

[15]Loth, J. L., and Boasson, M., "Circulation Control Optimization," *Journal of Aircraft*, Vol. 21, No. 2, 1984.

[16]Munro, S. E., Ahuja, K. K., Englar, R. J., "Noise Reduction Through Circulation Control," AIAA-2001-0666, Georgia Institute of Technology, GTRI/ATASL, Atlanta, GA, January 2008.

[17]Englar, R. J., Huson, G. G., "Development of Advanced Circulation Control Wing High-Lift Airfoils," David W. Taylor Naval Ship Research and Development Center, Bethesda, MD, January 1983.

[18]Englar, R. J., Williams, R. M., "Design of a Circulation Control Stern Plane for Submarine Applications," NSRDC TN AL-200, Naval Ship Research and Development Center, Bethesda, MD, March 1971.

[19]Abramson, J., Rogers, E. O., "High-Speed Characteristics of Circulation Control Airfoils," 83-0265 AIAA 21st Aerospace Sciences Meeting, David W. Taylor Naval Ship Research and Development Center, Bethesda, MD, January 1983.

[20]Lee-Rausch, E. M., Vatsa, V. N., Rumsey, C. L., "Computational Analysis of Dual Radius Circulation Control Airfoils," AIAA Paper 2006-3012, 2006.

[21]Lui, Y., "Numerical Simulation of the Aerodynamic Characteristics of Circulation Control Wing Sections," Ph. D. Dissertation, School of Aerospace Engineering, Georgia Institute of Technology, Atlanta, GA, 2003.

[22]Harlow, F. H., and Nakayama, P. I., "Transport of Turbulence Energy Decay Rate," Los Alamos, Science Laboratory, LA-3854, 1968.

[23]Spalart, P. R., and Allmaras, S. R., "A One-Equation Turbulence Model for Aerodynamic Flows," AIAA Journal Vol. 26, 1988, pp. 1299-1310.

[24]Wilcox, D. C., "Reassessment of the Scale-Determining Equation of Advanced Turbulence Models," AIAA Journal Val. 26, 1988, pp. 1299-1310.

[25]Chang, P. A., Slomski, J., Marino, T., Ebert, M. P., "Numerical Simulation of Two- and Three-Dimensional Circulation Control Problems," 43rd AIAA Aerospace Sciences Meeting and Exhibit, 2005.

[26]Jones, G. S., Lin, J. C., Allan, B. G., Milholen, W. E., Rumsey, C. L., Swanson, R. C., "Overview of CFD Validation Experiments for Circulation Control Applications at NASA," AIAA Paper 2008-030041, NASA Langley Research Center, Hampton, VA, 23681, 2008.

[27]Jones, G. S., Yao, C. S., and Allan, B. G., "Experimental Investigation of a 2D Supercritical Circulation-Control Airfoil Using Particle Image Velocimetry," AIAA Paper 2006-3009, June 2006.

[28]Marcos, J. M., "Computational and Experimental Comparison of a Powered Lift, Upper Surface Blowing Configuration," Accepted to 48th AIAA Aerospace Sciences Meeting, California Polytechnic State University, San Luis Obispo, CA, December 2009.

[29]Swanson, R. C., Rumsey, C. L., Anders, S. G, "Progress Towards Computational Method for Circulation Control Airfoils," AIAA Paper 2005-29, 2005.

[30]Bell, B., "Turbulent Flow Case Studies," Fluent Services Center, 2003.

[31] Storm, T. M., Marshall, D. D., "Assessing the v^2-f Turbulence Models for Circulation Control Applications," Accepted to 48th AIAA Aerospace Sciences Meeting, California Polytechnic State University, San Luis Obispo, CA, May 2009.

Appendix

	α = -5°	α = 0°	α = 3°
DR16	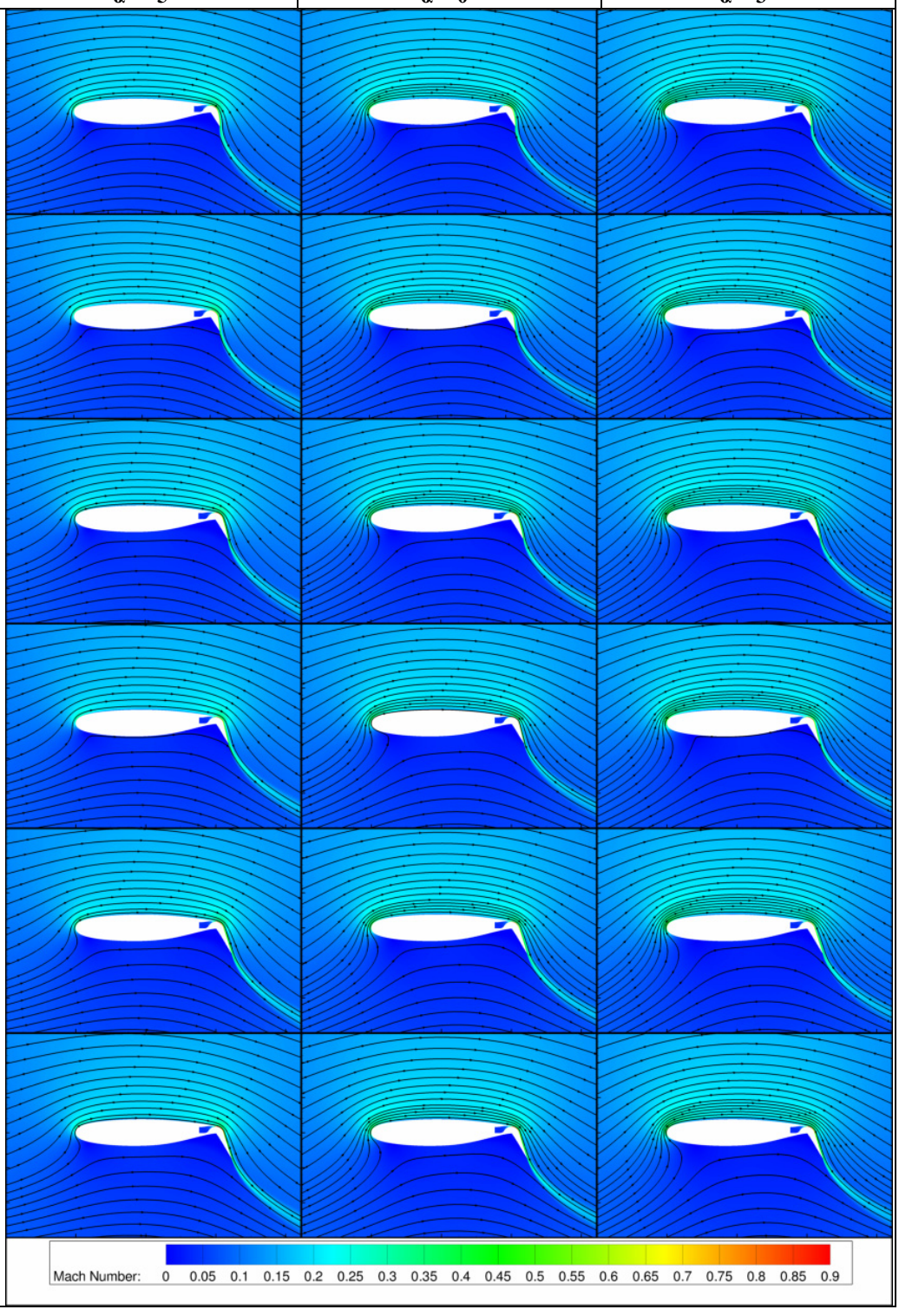		
PR16			
DR19			
PR19			
DR22			
PR22			